Journal of Materials Chemistry B

Accepted Manuscript

ROYAL SOCIETY OF CHEMISTRY

www.rsc.org/materialsB

Journal Name

RSCPublishing

ARTICLE

Probe spectrum measurements of Eu^{3+} ions as a relevant tool for monitoring *in vitro* hydroxyapatite formation in a new borate biomaterial

Shuyun Qi,[a] Yanlin Huang,[a*] Yadong Li,[a] Peiqing Cai,[b] Sun Il Kim,[b] Hyo Jin Seo[b*]

Cite this: DOI: 10.1039/x0xx00000x

Received ooth January 2012,
Accepted ooth January 2012

DOI: 10.1039/x0xx00000x

www.rsc.org/

CaB_2O_4 powders and ceramics were prepared by the conventional solid-state reaction. *In vitro* hydroxyapatite (HA) mineralization was investigated by soaking the samples in simulated body fluid (SBF) for various time periods. X-ray diffraction and structural refinements, scanning electron microscopy and X-ray energy-dispersive spectra measurements were applied to investigate apatite formation before and after immersion in SBF. HA can easy form flower-like nanostructure with nano-needles even soaked in SBF for several hours. The in vitro bioactivity of CaB_2O_4 was attributed to easy formations of B-OH groups in CaB_2O_4 structure soaked in SBF solutions. In the process of mineralization, the luminescence evolution of Eu^{3+} ions, a well-known structural probe, was detected by photoluminescence spectra and photoluminescence decay curves. This suggested that the process of mineralization can be monitored by the luminescence intensity of Eu^{3+} ions in the mineralization products. The current study will open up a new and simple in vivo avenue for in situ monitoring hydroxyapatite conversion with a fiber luminescence spectrometer.

Introduction

Bioactive inorganic materials have attached great attention for the use in specific clinical applications[1-4], for example, the demand for synthetic biomaterials to replace and repair bone tissue lost from injury or disease has significantly increased in the past years[5]. Hydroxyapatite ($Ca_{10}(PO_4)_6(OH)_2$, HA), as the major inorganic constituent of human hard tissues, has been widely used in bone and teeth repair due to its excellent bio-compatibility and osteoinductivity. A common characteristic of bioactive materials is the HA layers formation on the surface of materials when in contact with SBF (simulated body fluid) or dilute phosphate solution[6-8].

Ca-P based bio-ceramics such as HA, β-tricalcium phosphate (β-TCP) and HA/β-TCP, have been used as bone regeneration materials[9]. Although β-TCP materials have been regarded as biodegradable materials, the drawback of this material is its high degradation which resulted in mismatching with new bone formation. The degradation kinetic tends to be slow[6]. Many investigations have been paid on various new bioactive materials with good surface HA formation ability. For example, materials containing $CaO\text{-}SiO_2$ components have excellent bioactivity when immersed in SBF or implanted into the bone defect[10].

These materials including powders and ceramics have been widely investigated as potential candidate for bone tissue engineering applications such as Ca_2SiO_4 (powder and ceramic)[11,12], $CaSiO_3$ (powder and ceramic)[13-15], Zn_2SiO_4 (ceramic)[16], Ca_3SiO_5 (powder and ceramic)[17-19], $Ca_3Mg(SiO_4)_2$ (powder)[20], $Ca_2MgSi_2O_7$ (powder)[21], $Ca_7MgSi_4O_{16}$ (ceramic)[22-24], $CaMgSi_2O_6$ (powder and ceramic)[25,26], $Ca_2ZnSi_2O_7$ (powder)[27,28], $CaTiSiO_5$ (ceramic)[29,30], $Ca_3ZrSi_2O_9$ (ceramic)[31], $Ca_5(PO_4)_2SiO_4$ (powder and ceramic)[32], and $Ca_7Si_2P_2O_{16}$ (powder)[33], etc.

It is well-accepted that chemical compositions and crystal structure of the host materials directly exert great influence on the HA mineralization ability. The simultaneous dissolution of the host components and forming the HA nucleation in SBF are necessary. Various effects of inorganic boron B have been reported, including actions on reproduction and embryogenesis, improvement of wound healing, modifications of calcium, and bone metabolisms[34-36]. Borate has been recognized as an essential element for the growth both plants and animals. Boron supplementation in rats and chicks has been shown to increase bone strength[37]. It has been confirmed that boron components have a beneficial effect on bone formation, composition and physical characteristics[38]. For example, Silicate-based bioactive glasses undergo incomplete conversion to a calcium phosphate material after in vivo implantation, which severely limits their biomedical application[39]. However, Particles of a borate glass were fully converted to HA, whereas the silicate and borosilicate glasses were only partially converted to HA[40]. B-containing materials such as borosilicate glass[39], borate glasses[41], and sodium calcium borate glasses[42], are promising candidates for bone tissue engineering.

In our recent work, some calcium borates were investigated to develop possible biomaterials with apatite mineralization ability, such as calcium metaborate CaB_2O_4 reported here. Calcium metaborate is widely used in chemical industry in virtue of functions of fusion assistance, antiflaming, drying speedup, and sterilization. It is a raw material of nonalkali glass and performs better than boric acid. This metaborate is also used as prime paint of antirust paint, antiflaming paint, antifog agent, bactericide and catalyzer in

chemical industry[34]. Calcium metaborate can crystallize with four different structures by varying the pressure at which the synthesis is carried out, i.e., CaB_2O_4 (I,II, III, and IV)[34]. CaB_2O_4 II, III, and IV are high pressure phases grown at 20-30 kbar and 900 ^{0}C, and only CaB_2O_4(I) can be obtained at ordinary pressure[43]. CaB_2O_4 (IV) has a cubic structure of space group *Pa-3* and Ca ions are in 12 coordination[43]. CaB_2O_4 (III) has an orthorhombic structure with space group $Pna2_1$, and Ca ions are in 8- and 12- coordination[44]. CaB_2O_4 (II) has been determined by a metastable phase with a space group *Pccn* and 8-folod coordinated Ca ions[43]. Phase CaB_2O_4(I) is stable at atmospheric pressure. The structure was first investigated by Zachariasen in 1931[44] and refined thirty years later by Marezio et al[45]. It crystallizes in the orthorhombic structure and has a space group of *Pbcn* with *Z*=4. Ca ions are in 8-fold coordination.

In recent years, luminescence properties of RE (rare earth)-doped CaB_2O_4 have been paid more attention. The cut-off wavelength in CaB_2O_4 was reported to be about 190 nm[46]. CaB_2O_4:Eu^{2+} shows blue luminescence (410-445 nm) under the excitation of UV light[47,48]. Red-emitting phosphor of Eu^{3+}-doped CaB_2O_4 has been suggested to be a suitable candidate for the fabrication of near-UV InGaN based LED[49,50]. CaB_2O_4:Tb^{3+},Li^+ is a promising green-emitting phosphor, which matches well with the NUV- LED chips[51]. Recently, Fujimoto et al[46] reported the scintillation properties of 0.5% Ce^{3+}-doped CaB_2O_4 crystalline scintillator, which can find its application in the neutron detection.

The first motivation in this work is to investigate the bioactive ability for apatite mineralization in CaB_2O_4 powder and ceramic samples prepared by the solid-state reaction. The samples were introduced to soak in SBF to evaluate hydroxyapatite formation on surfaces by XRD, SEM and EDS measurements. The results indicate CaB_2O_4 has an excellent bioactivity and is a potential candidate of new biomaterials for hard tissue repair. The second motivation is to detect the luminescence properties of Eu^{3+}-doped CaB_2O_4 during the process of HA mineralization. Eu^{3+} is a well-known probe ion in the application of structure characterization and phase structure detection in luminescence materials. The spectral information was obtained in the transformation from CaB_2O_4 to HA, which is expected to monitor apatite mineralization process by photoluminescence method.

Experiments

Preparation of powder and ceramic samples

1.0 mol% Eu^{3+}-doped CaB_2O_4 powder and ceramic samples were prepared by using the conventional solid-state reaction. The starting materials were $CaCO_3$ (99.99%), Eu_2O_3 and H_3BO_3 (99.9%). Firstly, the stoichiometric materials were weighed and thoroughly mixed in an agate mortar, then transferred to a corundum crucible and heated at 350-450 °C for 5 h. Secondly, the mixtures were mixed again and heated at 800-850 °C for 5 h in air. Then, the mixture was thoroughly ball-milled using zirconia balls in plastic containers filled with ethanol for 24 h. CaB_2O_4 powder samples were obtained by directly heating the mixed powders in a covered platinum crucible at 850 °C.

To prepare the ceramic samples, the powders were compacted into disk-shaped ceramics (pellets) with 20 mm in diameter under a pressure of 50 kPa. PVA was added in the powders as organic binder to help the formation of cylindrical compacts. The binder-to-powder ratio was kept as 5/95 (w/w). The compacted pellets were subsequently heated at 850 °C for 10 h in air atmosphere using an electric furnace. That is to say, we obtained two kinds of samples, i.e., CaB_2O_4 powder and ceramics.

In vitro Bioactivity

Hydroxyapatite formation ability in the SBF is always used to evaluate the in vitro bioactivity of biomaterials for bone repair[52]. The sample was placed in a polystyrene bottles containing SBF with ion concentrations nearly equal to human blood plasma, which was prepared according to the procedure described by Kokubo and Takadama[53]. The bottle with SBF solution and CaB_2O_4 sample was incubated at 37.0 °C. After different soaking periods, the samples were removed from SBF, rinsed with deionized water, and dried at room temperature. After each soaking treatment, the sample was removed from the SBF and gently rinsed with deionized water and then dried in a drying oven. The surface structure and morphology of the specimens (powders and ceramic) before and after soaking in the SBF solution were characterized by X-ray diffraction and scanning electron microscopy (SEM) measurements. Compositional changes on cross-section of the samples were identified by SEM-associated energy-dispersive spectrum (EDS).

Characterization Techniques

XRD patterns of the as-synthesized and soaked samples were taken on a Rigaku D/Max diffractometer (Rigaku Co., Tokyo, Japan) operating at 40KV, 30mA with a Bragg-Brentano geometry using Cu Kα radiation (λ=1.5404 Å). The microstructure and the surface morphology of the powders and ceramics were investigated using scanning electron microscopy (JSM-6700F, JEOL Ltd., Tokyo, Japan) coupled with field emission (FE-SEM). The surface elemental analysis was performed by an energy dispersive spectrometer (EDS, JXA-8100, JEOL Ltd., Tokyo, Japan). The concentrations of Ca, P, and B in the collected SBF solutions were determined by inductively coupled plasma atomic emission spectroscopy (ICP-AES, Vista AX, Varian Co., America). The three-point bending strength (σ_f) and Young's modulus (*E*) were measured by a universal-testing machine (Instron-1195, USA) at a crosshead speed of 0.5 mm-min^{-1} and a span of 30.0 mm according to the ASTM C1259-95 standard[54]. The apparent densities were measured in water using the Archimedean technique and the relative densities were calculated from the apparent and true densities.

The photoluminescence (PL) excitation and luminescence spectra were recorded on a Perkin-Elmer LS-50B luminescence spectrometer with Monk-Gillieson type monochromators and a xenon discharge lamp, which was used as excitation source. In the PL measurements of the samples (powders or ceramics) can be fixed in the groove on the holder, which can be turned in 360 degree. For the measurements of luminescence and decay curves, the samples were excited by a pulsed Nd:YAG laser at 266 nm (Spectron Laser System SL802G). The luminescence was dispersed by the 75 cm monochromator (Acton-Research Corp. Pro-750) and multiplied by the PMT (Hamamatsu R928). The data were displayed and recorded with the LeCloy 9301 digital storage oscilloscope.

Results

Crystal formation and Microstructure of as-prepared samples

The as-prepared powders and ceramics were checked by powder XRD measurements, which were shown in Fig. 1. The XRD patterns can be well indexed according to the standard card No. 32-0155 for CaB_2O_4 selected in the International Centre for Diffraction Data (ICDD) database. No impurity XRD peaks were observed. All the samples show the pure CaB_2O_4 crystal phase. Based on the experimental XRD patterns, the structural parameters and atom positions of Eu^{3+}-doped CaB_2O_4 are refined by the GSAS (general structure analysis system) suite program of Rietveld method using CaB_2O_4 as initial model (PDF#2 No. 32-0155)[55]. The representative XRD structural refinements of CaB_2O_4:0.01Eu^{3+} are shown in Fig. 1, which plots experimental, calculated, and different results from the refinement.

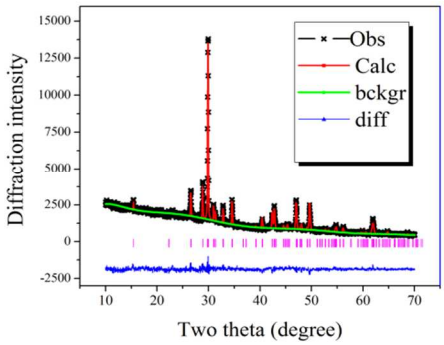

Fig. 1 Representative experimental (crossed) and calculated (red solid line) X-ray diffraction profiles of CaB_2O_4:0.01Eu^{3+}. The black with x marks is experimental pattern, and the red line with dots is the calculated one; the different profile is located at the bottom of the figure.

Table 1 Refined crystallographic parameters of CaB_2O_4:0.01Eu^{3+}

formula	CaB_2O_4
radiation	Cu Ka
2θ range (degree)	10-70
symmetry	orthorhombic
space group#	*Pbcn* (60)
a/Å	11.5905(12)
b/Å	4.2778(5)
c/Å	6.2134(7)
α/°	90
β/°	90
γ/°	90
Z	4
R_p (%)	0.0706
R_{wp} (%)	0.1265
X^2	1.844
V/$Å^3$	308.07 (9)

The refined parameters of Eu^{3+}-doped CaB_2O_4 are listed in Table 1. The host keeps good orthorhombic structure and the Eu^{3+} doping did not make significant changes to the crystal structure. The refinement parameters of the atomic coordinates and occupancies of CaB_2O_4:0.01Eu^{3+} are given in Table 2. The structure sketch map of CaB_2O_4 is shown in Fig. 2, which was modeled using the Diamond Crystal and Molecular Structure Visualization software on the basis of the atomic coordinate's refinements.

CaB_2O_4 compound crystallizes in the orthorhombic space group of *Pbcn* (No.60) and Z=4[44,45]. The framework of the structure is formed by triangular BO^{3-}groups that shared pairs of O-atoms generating infinite -O-B-O-B-O- chains running parallel to [001] presenting infinite $(BO_2)_\infty$ as shown in Fig. 2 (a). There are two types of chain construction, namely, one which consists of infinite $(BO_2)_\infty$ in triangularly coordinated borons, and $(CaO_8)_\infty$ of Ca atoms in 8-oxygen polyhedron. As shown in Fig. 2 (b), $(CaO_8)_\infty$ are connected by $(BO_2)_\infty$ chains[44,45]. The interesting feature of the structure is the presence of endless strings of BO_5 groups parallel to the c-axis. The oxygen atoms form an almost equilateral triangle around each boron atom. The B-O distances are: 1.35 Å, 1.35 Å and 1.38 Å[56]. All the BO_3 groups are oriented parallel to the *a*-face.

Table 2 Refined atomic coordinate parameters of CaB_2O_4:0.01Eu^{3+}

Atom	Wyck.	Site	x/a	y/b	z/c	U [$Å^2$]
Ca	4c	2	0	0.2619(30)	1/4	0.0386(22)
O1	8d	1	0.41372	0.22921	0.0919	0.0003
B	8d	1	0.2969(20)	0.332(6)	0.1315	-0.025(6)
O2	8d	1	0.20786	0.15249	0.1483	0.0003

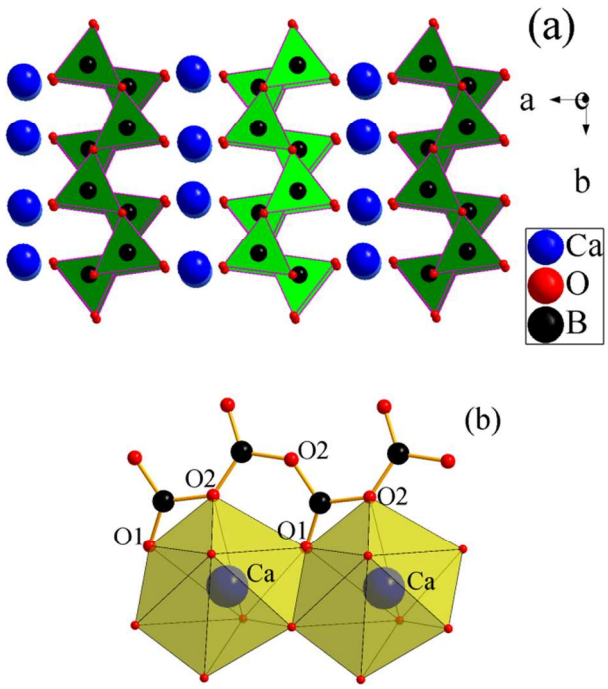

Fig. 2 (a): Schematic views of the structure of CaB_2O_4 along the c-direction; (b): a section of one of the endless strings of BO_3 groups viewed along the a-axis.

Fig. 3 (a) shows the representative SEM micrograph of as-prepared CaB_2O_4 powders. The powder samples have an irregular shape with very stiff boundary. The particle size of the powders can be estimated to be about 3-10 μm. There was no aggregation of the CaB_2O_4 particles. Fig. 3 (b) shows the SEM micrograph of as-prepared CaB_2O_4 ceramics. The ceramics were not completely dense and the relative density was about 92.5%. The crystal grains were not observed on the surface of the ceramics. It is obvious that the surfaces of both the powders and the ceramics are very smooth and clean.

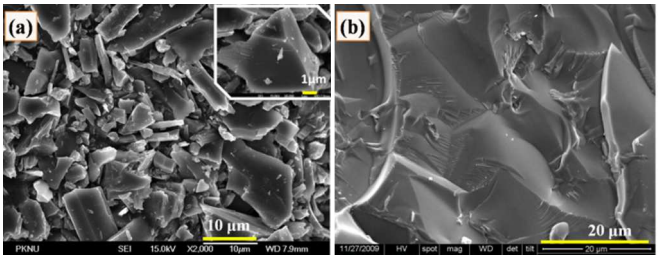

Fig. 3 SEM micrographs of the as-prepared CaB_2O_4 powders (a) and ceramics (b).

The bending strength of CaB_2O_4 ceramic was measured to be 96.5 MPa, which is higher than the reported value for HA ceramics (84.4 MPa)[32]. While the elastic modulus of CaB_2O_4 ceramic (83.5 GPa) is lower than that of HA ceramics (97.7 GPa)[32]. As compared to the HA ceramic, the CaB_2O_4 ceramic revealed the improved mechanical properties.

HA formation after soaking CaB_2O_4 in SBF

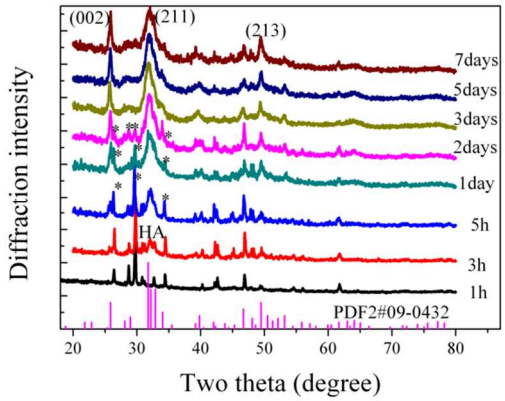

Fig. 4 XRD patterns of CaB_2O_4 soaked in SBF solutions for different time-periods labeled on the figure. The patterns are compared with the PDF2 standard card No: 09-0432 (HA). The asterisks denote the remnant CaB_2O_4 peaks.

XRD measurements were used to confirm the formation of hydroxyapatite on the surfaces of CaB_2O_4 samples after immersion in SBF solution. Fig. 4 shows XRD patterns of the CaB_2O_4 ceramics after soaking in SBF for various time periods. The powder samples have the similar patterns. As observed in Fig. 1, the as-prepared samples show a pure CaB_2O_4 crystal phase. After soaking in SBF, the characteristic peaks of CaB_2O_4 decreased and the new peaks such as (002), (211) and (213) corresponding to the reflection of HA (PDF#09-0432) can be observed. This indicates that the conversion of the CaB_2O_4 to HA in SBF had occurred. With increasing soaking time for 1, 2, 3 and 5 days, the intensity of HA XRD peaks increased. This indicates that there are more HA layers depositing on the surface of the CaB_2O_4 samples. The characteristic peaks of CaB_2O_4 completely disappeared after soaking in SBF for 3 days. It is obvious that the characteristic peaks of HA can begin to appear even after 3h of the soaking. As the results described above, CaB_2O_4 materials could develop a hydroxyapatite layer on the surface.

Microstructure of the formed HA

Fig. 5 and 6 show SEM micrographs of the CaB_2O_4 powder and ceramic samples after soaking in SBF, respectively. In comparison with the morphology of the as-prepared samples as shown in Fig. 3, great changes can be observed in the samples after soaking in the SBF solutions. After soaking in the SBF for 1 day, the CaB_2O_4 ceramic (Fig. 5 a) and powder (Fig. 6 a) host could hardly be seen. The surfaces of both the powder and the ceramics became very coarse, on which some tiny sediment could be observed. The newly formed layer was suggested to be HA confirmed by the XRD measurements in Fig. 4.

The higher magnification scanning electron microscopy (SEM) micrographs of the CaB_2O_4 ceramics (Fig. 5 a) and powder (Fig. 6 b) samples reveal that myriads of fluff-like agglomerated HA fibers on the surface of the samples. The soft fibrous nano-crystallites formed a carpet-like with a fine structure overgrow on the surface. The length and radius of the uniform nano-fibers are estimated to be 500 nm and 10 nm, respectively.

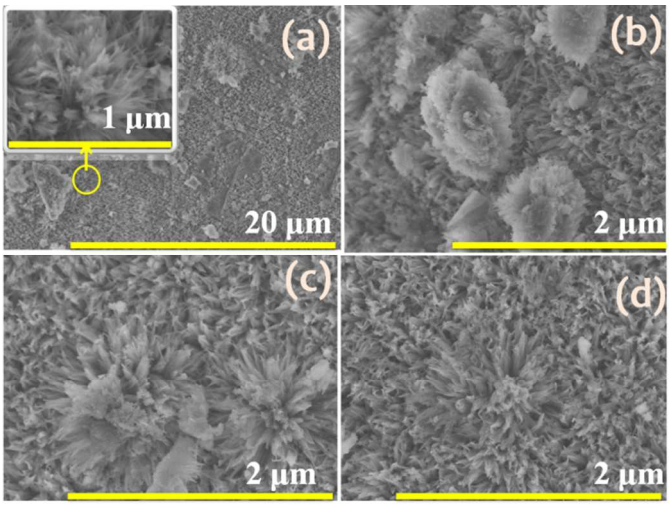

Fig. 5 (a): SEM micrographs of CaB_2O_4 ceramics soaked in SBF for 2 days; (b): typical HA flower-buds; (c): typical HA Flowers in bloom; (d): typical HA flowers in full bloom.

The experiments indicate that the HA nano-fibers look like soft flowers. At the beginning of the mineralization such as several hours to 2 days, HA flower-buds can be formed as shown in Fig. 5 (b). The HA flower gradually bloom with the increase of soaking time in SBF for 3 days as shown in Fig. 5 (c). Fig. 5 (d) shows that the HA flowers can be in full bloom after soaking the samples in SBF for 5 days. Lu et al[32] have reported that few bone-like hydroxyapatite precipitated on the HA ceramic samples even after soaking in SBF for 7 days. The results indicate that CaB_2O_4 biomaterials show good surface HA formation ability. Meanwhile, the FWHM of the XRD peaks in Fig. 4 seems to be broader with increase of soaking time. This could be due to the incomplete or defective crystals, decrease of the particle size. It is found that the nanoparticles get smaller size and more fine fibers-like shape on the HA layer. It has been reported that the increase of time and carbonate concentration can decrease the HA size and yield more needle-like grain shapes in the reaction of sodium calcium borate glasses to form HA[42].

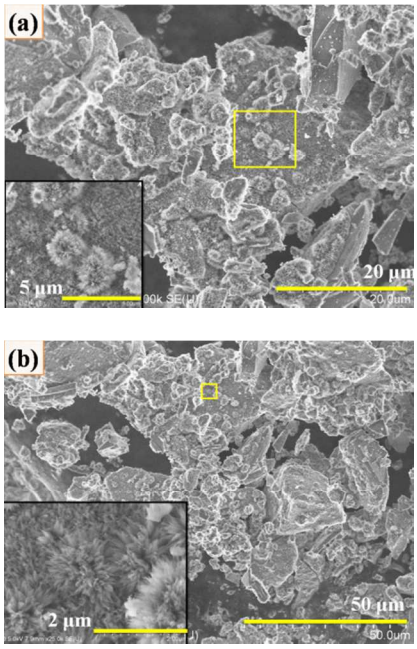

Fig. 6 Typical SEM micrographs of CaB_2O_4 powder samples soaked in SBF for 1 day (a) and 3 days (b).

Chemical formation of HA layers

EDS measurements were used to examine the elemental compositions on the surface of the soaked samples. The representative EDS spectra and the elements of the samples soaked in SBF solutions for 1, 3, 5, and 7 days are shown in Fig. 7. Several specific lines show the signals of Ca, O, B, and Eu elements in the samples. The quantificational ratio for the elements was listed in Fig. 7. After soaking in SBF for 1 day (Fig. 7 a), new chemical component P can be detected and the average Ca/P ratio was calculated to be 2.38. This indicates that the P element in SBF solutions deposited on the surface of the sample joining in HA.

After immersing in SBF for a longer time, a successive hydroxyapatite layer was formed on the surface of the material surface. It showed an average Ca/P ratio are 1.97 and 1.67 for the sample soaked for 3 (Fig. 7 b) and 5 days (Fig. 7 c), which is close to the theoretical stoichiometric value of 1.67 in HA. The Ca/P molar ratio decreased abruptly to 1.59 after soaking in SBF for 7 days. This ratio is slightly lower than the theoretical stoichiometric value of 1.67, which has often been reported for the hydrothermally synthesized HA and is more similar to that of natural bone minerals[57]. The formation of hydroxyapatite on the CaB_2O_4 surface indicates that this calcium borate possess good interface bioactivity.

The ion concentrations in final solutions were also analyzed. Changes in element concentrations of calcium, borate and phosphorus in the collected SBF immersed with CaB_2O_4 samples for various periods are shown in Fig. 8. Calcium ions (Ca) and borate ions (B) were released from CaB_2O_4 while P concentration decreased due to the formation of HA onto the samples. Generally, the change of the ion concentration in solution confirmed the precipitation of HA.

It is obvious that the ion concentrations of SBF solutions changed markedly after 1 day of soaking. The calcium and borate concentrations in SBF have a rapid increase, while P concentration gradually decreased at the early stage of immersion of the samples.

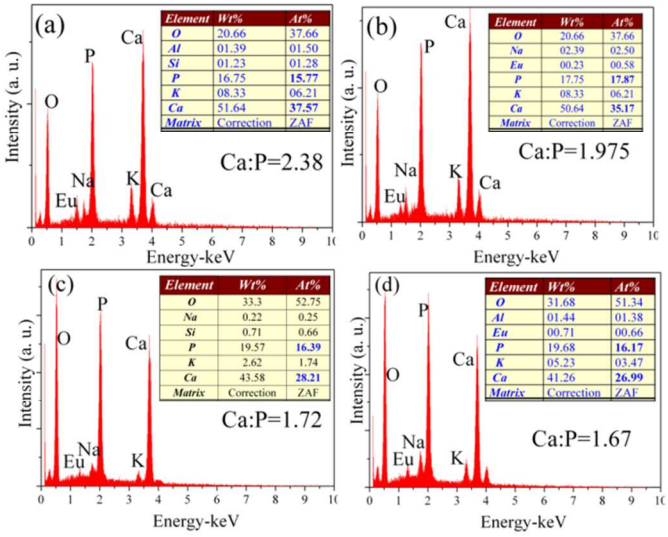

Fig. 7 Typical X-ray EDS spectra of CaB_2O_4 samples soaked in SBF solutions for 1 day (a), 3 days (b), 5 days (c), and 7 days (d). Inset shows the quantificational ratio of the elements calculated from EDS data.

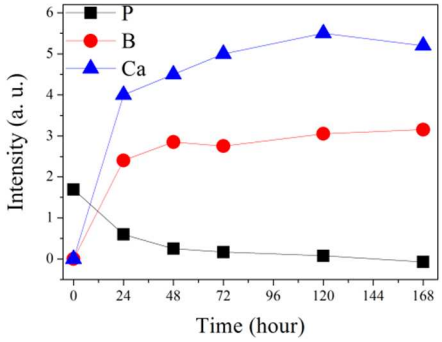

Fig. 8 Changes of Ca, B, and P concentrations in SBF solutions measured after soaking the CaB_2O_4 samples for various periods.

Luminescence characteristic and its evolution in the process of HA mineralization

Fig. 9 presents the emission spectrum of as-prepared Eu^{3+}-doped CaB_2O_4 ceramic under the excitation of UV light 254 nm. The groups of sharp peaks are from the luminescence transitions of $^5D_0 \rightarrow {}^7F_J$ (J=0, 1, 2, 3 and 4) levels of Eu^{3+} ions. The emission at about 580 nm is the transition $^5D_0 \rightarrow {}^7F_0$.

The orange emission of 585 and 597 nm are assigned to the magnetic dipole transition of $^5D_0 \rightarrow {}^7F_1$. The red emissions at 610, 621 nm are ascribed to electric dipole transition of $^5D_0 \rightarrow {}^7F_2$. The emission corresponding to the transition of $^5D_0 \rightarrow {}^7F_{3,4}$ is weak. This result is in agreement with the reports[49,50] in CaB_2O_4:Eu^{3+} phosphor.

According to the Judd-Ofelt theory[58,59], if Eu^{3+} ions occupy an inversion symmetry site, magnetic transition $^5D_0 \rightarrow {}^7F_1$ is dominant. Otherwise, the electric dipole transition $^5D_0 \rightarrow {}^7F_2$ is the dominant transition. The magnetic dipole transition $^5D_0 \rightarrow {}^7F_1$ of Eu^{3+} is dominant in CaB_2O_4 indicating the Eu^{3+} does occupy the inversion symmetry site in the host lattice according to the Judd–Ofelt theory.

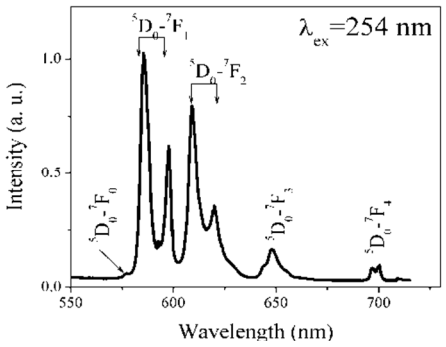

Fig. 9 Photoluminescence spectrum of as-prepared Eu^{3+}-doped CaB_2O_4 ceramic under the excitation of UV light 254 nm.

The photoluminescence spectra of Eu^{3+}-doped CaB_2O_4 were detected after HA mineralization for different time periods. In this experiment the relation between the luminescence intensity and the soaking time was difficult determined because the usually the excitation light only penetrates very thin depth on the surface. Our intention is to find some spectral characteristics of Eu^{3+}, which is a well-known probe ion to show the structural characteristics. This is expected to monitor the in vivo mineralization dynamic process of bioactive materials with some assistance such as an optical fiber. Fig. 10 shows luminescence spectra of Eu^{3+}-doped CaB_2O_4 after HA mineralization for different periods. The spectra and its evolution during the HA mineralization have the following characteristics.

Firstly, the evolution of HA crystallization can be monitored by the intensity ratio between the luminescence transitions ($^5D_0 \rightarrow {}^7F_2$) and ($^5D_0 \rightarrow {}^7F_1$) of Eu^{3+} ions.

It is well known that according to the Judd-Ofelt theory, the forced electrical dipole transition $^5D_0 \rightarrow {}^7F_2$ is very sensitive to the local environment, while the magnetic dipole transition $^5D_0 \rightarrow {}^7F_1$ is not much affected by the ligand field around Eu^{3+} ions[60]. If Eu^{3+} ions occupy an inversion symmetry site, the orange-red emission, magnetic transition $^5D_0 \rightarrow {}^7F_1$ is the dominant transition. On the contrary, electric dipole transition $^5D_0 \rightarrow {}^7F_2$ is the dominant transition[61]. Therefore, the intensity ratio of $R=I(^5D_0 \rightarrow {}^7F_2)/I(^5D_0 \rightarrow {}^7F_1)$ is a measure of Eu^{3+} ion's site symmetry. A higher symmetry of the crystal field around Eu^{3+} will result in a smaller value[60].

The photoluminescence spectra of Eu^{3+}-doped CaB_2O_4 after HA mineralization for different time periods are displayed in Fig. 10 (a). The R value for each spectrum is shown in Fig. 10 (b). It is clear that the R value (about 1) of the as-prepared sample has an abrupt increase when the sample was mineralized in SBF (R=5). The higher R values indicate a considerably distorted crystallographic environment of Eu^{3+} in the HA layers. This can be seen from the very broad emission spectra for each sample soaked in SBF for 1 h to 1 day. With the increase of soaking time, R value gradually decreases. As seen in Fig. 10 (a), the emission peaks for ($^5D_0 \rightarrow {}^7F_2$) and ($^5D_0 \rightarrow {}^7F_1$) transition of Eu^{3+} ions present nearly the same intensity on the emission spectra for 5 and 7 days soaking. This indicates that the newly formed HA crystals obtained high crystallization. In return we can use R as a sign to know the process of a HA mineralization process.

Secondly, $^5D_0 \rightarrow {}^7F_4$ transition has different intensity at the various soaking time in SBF

Figure 10 (c) shows the integrated intensity ($^5D_0 \rightarrow {}^7F_4$) of Eu^{3+} ions in each spectrum. It is shown that ($^5D_0 \rightarrow {}^7F_4$) increase its intensity with extending the soaking time in SBF. In Fig. 10 (a), a distinct luminescence property of the Eu^{3+}-doped sample soaked in SBF for 5-7 days is the strongest intensity of $^5D_0 \rightarrow {}^7F_4$ transition. This is also different from the usually reported results in Eu^{3+}-doped phosphors, which show the emission spectra with the predominated transition $^5D_0 \rightarrow {}^7F_2$ or $^5D_0 \rightarrow {}^7F_1$ of Eu^{3+} ions.

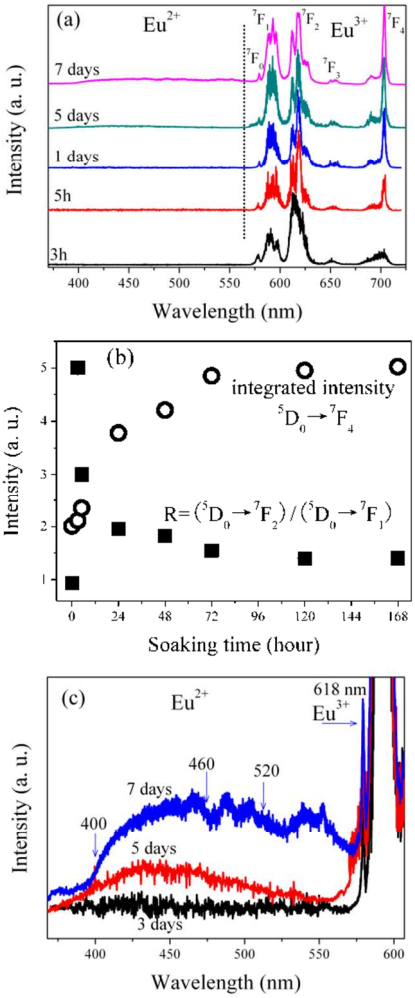

Fig. 10 (a): Photoluminescence spectra (λ_{ex}=254 nm) of Eu^{3+}-doped CaB_2O_4 ceramic after HA mineralization for different time periods; (b): the intensity ratio of luminescence transitions of ($^5D_0 \rightarrow {}^7F_2$)/($^5D_0 \rightarrow {}^7F_1$) and the integrated intensity ($^5D_0 \rightarrow {}^7F_4$) of Eu^{3+} ions; (c): the enlargement of the spectra in 350-600 nm.

The similar abnormal $^5D_0 \rightarrow {}^7F_4$ intensity has been reported in $Na_9[EuW_{10}O_{36}]$[62], $LaBWO_6$:Eu^{3+}[63], $(Y_3A_{l4-x}Ga_{1-x}O_{12})$:$Eu^{3+}$[64] and β-$Ca_2SiO_4$:$Eu^{3+}$[65]. In tungstate $Na_9[EuW_{10}O_{36}]$, it was suggested due to a highly polarizable chemical environment with local symmetry in corresponding to a distorted coordination polyhedron[62]. In Eu^{3+}-doped $LaBWO_6$[65], it was suggested due to a highly polarizable chemical environment corresponding to a coordination polyhedron. In Eu^{3+}-doped $(Y_3A_{l4-x}Ga_{1-x}O_{12})$, Skaudzius et al[64] discussed the dominated $^5D_0 \rightarrow {}^7F_4$ transitions with regard to the influence of site

symmetry, electronegativity (EN) and ionic radius of M^{3+} cations in the host (M=Al, Ga, and Y). The fraction of $^5D_0 \rightarrow {}^7F_4$ transition with respect to the whole emission spectrum increases with increasing average EN values of M^{3+} ions[64]. The environment of Eu^{3+} ions is more polarized while the cations in the compound have lower EN. In present work, this abnormal intensity has not a clear explanation; however, it is reasonable that the environment around Eu^{3+} ions could be influenced by the nature lattice of host

Thirdly, at final stage of mineralization, Eu^{2+} ions can be formed in the HA layers even this is processed in air atmosphere.

Figure 10 (c) is the enlargement of the spectra in 350-600 nm wavelength regions. Except for the emission peaks from Eu^{3+} ions, the very broad emission band from 380 nm to 580 nm can be observed. To identify this emission band, we detected the luminescence decay curves in the spectra as shown in Fig. 11. This emission band is assigned to the $4f^7$-$4f^65d$ transition of Eu^{2+} ions in the HA layer by the following reasons:

(1) According to references, the emission $4f^7$-$4f^65d$ positions of Eu^{2+} ions in CaB_2O_4 usually locate in the blue wavelength region 370 nm and 445 nm[47,48]. By comparing the spectral characteristics of the emission bands in Fig. 10 (c) with the reported CaB_2O_4:Eu^{2+}, it is easily seen that the shapes and positions of the emission bands are totally different, that is the broad emission bands which are not from the Eu^{2+} ions in residual CaB_2O_4 host.

(2) Usually, the decay time of electric-dipole allowed transition of $4f^65d^1 \rightarrow 4f^7$ is not longer than 1 μs[66]. Fig. 11 shows the luminescence decay curves of Eu^{3+} (618 nm) and Eu^{2+} (400, 460, 520 nm). The $^5D_0 \rightarrow {}^7F_2$ emission transition from Eu^{3+} ions shows an exponential decay curve (inset Fig. 11), which can be fitted using the function:

$$I = A\exp(t/\tau) \quad (1)$$

where I is the phosphorescence intensity at time t, A is constant, and τ is the decay time. The $^5D_0$ state of Eu^{3+} has a long lifetime of 2.5 ms. The emission from Eu^{2+} presents a nonexponential curve, indicating this activator could provide an extra decay channel. The decay can be fitted to the effective lifetime defined as the following:

$$\tau_{average} = \frac{\int_0^\infty I(t)tdt}{\int_0^\infty I(t)dt} \quad (2)$$

where *I(t)* represents the luminescence intensity at time *t* after the cutoff of excitation. The broad emission band show very short lifetime of 16-19 ns. The emission spectra under short decay time show dominate band from Eu^{2+}.

(3) In 2010, Graeve et al[67] reported the detailed analysis of the luminescence behavior of Eu^{3+}-doped hydroxyapatite (HAp) and calcium-deficient hydroxyapatite (Ca-D HAp). For the HAp:Eu powders, the emission is clearly from Eu^{3+} ions and corresponds to typical $^5D_0 \rightarrow {}^7F_J$ emissions, whereas for the Ca-D HAp:Eu powders, a broad emission bands corresponding to the $4f^65d^1 \rightarrow 4f^7$ ($^8S_{7/2}$) transition of Eu^{2+} were detected. This has been discussed that the substitution of Eu^{3+} on Ca^{2+} ions requires a charge compensation that forces the removal of a proton from the structure.

The energy required to remove the protons from the structure might be too high, resulting in a significant amount of Eu^{2+} in the Ca^{2+} sites of the crystal. Later Feng et al[68] confirmed the Graeve's results by the luminescence investigations in Eu-doped calcium-deficient hydroxyapatite $Ca_{8.95}Eu_{0.05}HPO_4(PO_4)_5OH$ prepared via the co-precipitation method and calcined in air. The emission spectra showed a broad emission band from the typical $4f^65d^1 \rightarrow 4f^7$ transition of Eu^{2+} ions, and sharp peaks corresponded to the $^5D_0 \rightarrow {}^7F_J$ (J=0, 1, 2, 3, 4) transitions of Eu^{3+} ions. In our experiment, the sample soaked in SBF for 7 days shows clear Ca deficient due to the EDS measurements in Fig. 7 (d). According to the reported results mentioned above, it is reasonable to ascribe the broad emission band to Eu^{2+} ions in HA, which have deficient Ca deviating from stoichiometric chemical of HA layers.

Discussions

Due to the results shown above, it can be noted that CaB_2O_4 compounds have a good HA mineralization in SBF. It has been reported that the prerequisite for hydroxyapatite formation on an implantable material in a living body is the presence of a type of functional group that could act as effective sites for hydroxyapatite nucleation on its surface[69]. The process of mineralization in a bioactive ceramic belongs to dissolution and deposition reaction. To form HA layers on the sample surface, the biomaterials comprising Ca-elements must release Ca^{2+} ions for HA formation on the surfaces. Consequently the simultaneous dissolution of the matrix materials in the interface between the host and the SBF solutions is necessary for the formation of the HA nucleation and crystal formation[70]. For example, in the reported mineralization process in a $CaO–SiO_2$ component, the first step is a part of Si-O-Si fracture forming Si–OH groups on the surface. Then Si^{4+}, Ca^{2+} ions get into the solution gradually, and form a hydrated layer at the beginning of mineralization[71]. This is followed by Ca^{2+} and PO_4^{3-} ions being absorbed from body fluids forming an amorphous Ca-P deposition on the surface of the ceramic. With increased implantation time, a crystallized Ca–P (apatite) phase forms.

In the present work, CaB_2O_4 exhibited a greater in vitro apatite-forming ability. First of all, this is attributed to its special crystal structure. The compound of CaB_2O_4 was investigated for the structural characteristic using powder XRD refinement as shown in Fig. 1. As shown in the schematic structure of CaB_2O_4 in Fig. 2, the linkage pattern of the BO_3 groups by the Ca atoms is regular. The framework is composed of the presence of calcium as polyhedron CaO_8 and triangularly coordinated boron as (BO_3) groups in lattices[44,45]. The interesting feature of the structure is that the triangular BO_3 groups share pairs of O^{2-} generating the endless -O-B-O-B-O- infinite chains $(BO_2)_\infty$ running parallel to [001][56].

Note that the BO_3 groups in CaB_2O_4 lattices are thermodynamically more unstable than those of SiO_4, PO_4 or BO_4 groups. The structural characteristics are favorable for the release of Ca^{2+} ions into SBF for an easy nucleation of hydroxyapatite on the surface of the crystal. BO_3 units provide more favorable sites for the release of B^{3+} than that in BO_4 tetrahedra. After soaking CaB_2O_4 in SBF, BO_3^{3-} ions are easily released into the surrounding solution. It is easy formation of B-OH groups in CaB_2O_4 structure soaked in SBF. The released BO_3^{3-} ions could improve the supersaturation of the SBF. This gives a high bioactive nucleation of hydroxyapatite layer on the surface of the CaB_2O_4 samples.

For HA mineralization in Ca-containing ceramic the dissolution and deposition reaction in SBF should take place successively. In CaB_2O_4 lattices the Eu^{3+} ions are substitute Ca sites forming (EuO_8) in the $(CaO_8)_\infty$ connected with BO_3 chains (Fig. 2). Compared with SiO_4, PO_4 or BO_4, BO_3 groups are easier to release from the lattices in CaB_2O_4 lattices. It can be suggested that it is easy to release $Ca(Eu)O_8$ in the lattices for HA formation on the surfaces. Ca(Eu) ions get into the solution and form a hydrated layer, which are absorbed from SBF forming an amorphous Ca-P deposition on the surface. In this process EuO_8 can be implanted in apatite crystal.

There are two sites of M(I) and M(II) in apatite $M_{10}(PO_4)_6X_2$ (*M*=Ca, Sr, Ba; *X*=F, Cl, Br, OH): M(I), 4f sites with C_3 symmetry, are surrounded by nine oxygen atoms; M(II), 6h site with C_s symmetry, are surrounded by six oxygen atoms and one *X* ion[72]. Previous studies have reported that RE ions are mainly doped at M(II) sites[73,74]. For dopant Eu^{2+} ions, two Eu^{2+} sites are reported: 340-380 nm for Eu^{2+}(Ca)I and 420-450 nm for Eu^{2+}(Ca)II[75]. Comparison with the reported wavelength for Eu^{2+}-doped apatites, the Eu^{2+} bands observed in the Fig. 10 shift to higher wavelength at 460 and 520 nm. The red-shift can be explained by the influence of structural disorder, i.e., the Eu^{2+} ions could experience stronger crystal field strength leading to the longer wavelength emission.

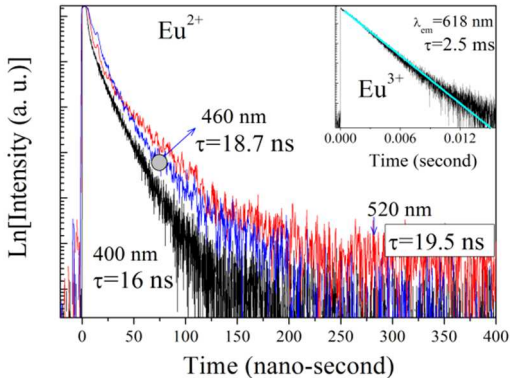

Fig. 11 Luminescence decay curves by monitoring the emission wavelength from Eu^{2+} and Eu^{3+} labeled in Fig. 10 (c).

For the luminescence results in this work, we could propose that such a fluorescence measurement is expected to be a new method in qualitatively determining the phase composition of Eu-doped hydroxyapatite powders, ceramics. This could be applied by the assistance of optical fiber to detect the luminescence signal to present the information In vitro hydroxyapatite formation in specific clinical applications for bone therapy. Certainly many investigations should be continued in the next work, such as the in vivo biocompatibility.

Conclusions

A new bio-material of CaB_2O_4 was prepared by the conventional solid-state reaction, which possess *in vitro* apatite mineralization ability. After soaking in SBF a crystalline HA layer can be formed on the surface of the sample, which was composed by HA nano-fibres or nano-needles with flower-like nanostructure. The results indicate that the biomaterials based on CaB_2O_4 might be a potential candidate as biomaterials for hard tissue repair. The structure of CaB_2O_4 containing BO_3 groups is favorable for formation of apatite mineralization on the surface of the samples. The luminescence evolution of Eu^{3+} ions was applied to monitor the mineralization process in 1.0 mol% Eu^{3+}-doped CaB_2O_4. Before mineralization, the emission showed a dominated $^5D_0 \rightarrow {}^7F_1$ transition. After soaking in SBF, three new spectral characteristics were detected: Firstly, there are obvious changes of the intensity ratio between the luminescence transitions ($^5D_0 \rightarrow {}^7F_2$) and ($^5D_0 \rightarrow {}^7F_1$) of Eu^{3+} ions; Secondly, $^5D_0 \rightarrow {}^7F_4$ transition presents unusual intensity; thirdly, at final stage of mineralization, Eu^{2+} ions can be detected. The results suggests that the mineralization process can be monitored by the luminescence of $Eu^{3+,2+}$ ions in the products. The current study would open up a new and simple method for *in situ* monitoring HA conversion with the assistance of an optical fiber and a spectrometer.

Acknowledgements

This research was supported by Basic Science Research Program through the National Research Foundation of Korea (NRF) funded by the Ministry of Science, ICT & Future Planning (NRF-2013R1A1A2009154) and by the Priority Academic Program Development of Jiangsu Higher Education Institutions (PAPD), China.

Notes

[a] *College of Chemistry, Chemical Engineering and Materials Science, Soochow University, Suzhou 215123, China, huang@suda.edu.cn (Yanlin Huang).*
[b] *Department of Physics and Center for Marine-Integrated Biomedical Technology, Pukyong National University, Busan 608-737, Republic of Korea, E-mail: hjseo@pknu.ac.kr (Hyo Jin Seo) Tel.: +82-51-629 5568; Fax:+82-51-6295549*

References

1 A. J. Salinas and M. Vallet-RegÍ, *RSC Advan ces*, 2013, 3, 11116-11131.
2 C. Zhong and C. C. Chu, *J. Mater. Chem.*, 2012, 22, 6080-6087.
3 N. M. Alves, I. B. Leonor, H. S. Azevedo, R. L. Reis, J. F. Mano, *J. Mater. Chem.*, 2010, 20, 2911-2921.
4 M. Vallet-Regí, M. Colilla, and B. González, *Chem. Soc. Rev.*, 2011, 40, 596-607.
5 Z. Xia, M. M. Villa and M. Wei, *J. Mater. Chem. B*, 2014, 2, 1998-2007.
6 S. F. Xu, K. L. Lin, Z. Wang, J. Chang, L. Wang, J. X. Lu, *Biomate*, 2008, 29, 2588-2596.
7 M. Xu, Y. Zhang, D. Zhai, J. Chang, C. T. Wu, *Biomaterials Science*, 2013, 1, 933-941.
8 Y. He, X. Wang, L. Chen, J. D. Ding, *J. Mater. Chem. B*, 2014, 2, 2220-2227.
9 A. El-Ghannam, P. Ducheyne and I. M. Shapiro, *Biomater*, 1997, 18, 295-303.
10 H. Oonishi, L. L. Hench, J. Wilson, F. Sugihara, E. Tsuji, M. Matsuura, *J Biomed Mater Res*, 2000, 51, 7-46.

11 Z. Gou and J. Chang, *J Eur Ceram Soc*, 2004, 24, 93-99.
12 Z. R. Gou, J. Chang and W. Y. Zhai, *J Eur Ceram Soc*, 2005, 25, 1507-1514.
13 C. T. Wu, Y. Ramaswamy, P. Boughton, H. Zreiqat, *Acta Biomater*, 2008, 4, 343-353.
14 S. Ni, J. Chang and L. Chou, *J Biomed Mater Res A*, 2006, 76, 196-205.
15 K. L. Lin, J. Chang, Y. Zeng, W. J. Qian, *Mater Lett*, 2004, 58, 2109-2113.
16 M. L. Zhang, W. Y. Zhai and J. Chang, *J Mater Sci Mater Med*, 2010, 21, 1169-1173.
17 W. Y. Zhao, J. Y. Wang, W. Y. Zhai, Z. Wang, J. Chang, *Biomater*, 2005, 26, 6113-6121.
18 W. Y. Zhao, J. Chang, J. Y. Wang, W. Y. Zhai, Z. Wang, *J Mater Sci Mater Med*, 2007, 18, 917-923.
19 W. W. PengB, W. N. Liu, W. Y. Zhai, L. Jiang, L. F. Li, J. Chang, *J Endod*, 2011, 37, 1240-1246.
20 M. Hafezi-Ardakani, F. Moztarzadeh, M. Rabiee, A. R. Talebi, *Ceram Inter*, 2011, 37, 175-180.
21 C. T. Wu and J. Chang, *J Biomater Appl*, 2007, 21, 251-263.
22 C. T. Wu, J. Chang, J. Y. Wang, S. Y. Ni, W. Y. Zhai, *Biomater*, 2005, 26, 2925-2931.
23 Y. Miake, T. Yanagisawa, Y. Yajima, H. Noma, N. Yasui, T. Nonami, *J Dent Res*, 1995, 74, 1756-1763.
24 C. T. Wu, J. Chang, W. Y. Zhai, S. Y. Ni, *J Mater Sci Mater Med*, 2007, 18, 857-864.
25 C. T. Wu and H. Zreiqat, *Acta Biomater*, 2010, 6, 820-829.
26 C. T. Wu, Y. Ramaswamy and H. Zreiqat, *Acta Biomater*, 2010, 6, 2237-2245.
27 Y. Ramaswamy, C. T. Wu, H. Zhou and H. Zreiqat, *Acta Biomater*, 2008, 4, 1487-497.
28 H. X. Lu, N. Kawazoe, T. Tateishi, G. P. Chen, X. G. Jin, J. Chang, *J Biomater Appl*, 2010, 25, 39-56.
29 C. T. Wu, Y. Ramaswamy, X. Y. Liu, G. C. Wang, H. Zreiqat, *J R Soc Interface*, 2009, 6, 159-168.
30 Y. Ramaswamy, C. T. Wu, C. R. Dunstan, B. Hewson, T. Eindorf, G. I. Anderson, *Acta Biomater*, 2009, 5, 3192-3204.
31 Y. Ramaswamy, C. T. Wu, A. V. Hummel, V. Combes, G. Grau, H. Zreiqat, *Biomater*, 2008, 29, 4392-4402.
32 W. H. Lu, W. Duan, Y. P. Guo, C. Q. Ning, *J Biomater Appl*, 2010, 26, 637-650.
33 Y. H. Zhou, C. T. Wu and Y. Xiao, *Acta Biomater*, 2012, 8, 2307-2316.
34 X. L. Cheng, F. F. Dong and C. Yu, Struct Chem, 2009, 20, 221-226.
35 M. Dzondo-Gadet, R. Mayap-Nzietchueng, K. Hess, P. N Abet, F. Belleville, B. Dousset, Humana of Boron at the Molecular Level Effects on Transcription and Translation in an Acellular System, *Biological Trace Element Research*, 2002, 85, 23-33.
36 F. Jay Murray, A Comparative Review of the Pharrnacokinetics of Boric Acid in Rodents and Humans, *Biological Trace Element Research*, 1998, 66, 331-341
37 Tara A. Devirian and Stella L. Volpe, The Physiological Effects of Dietary Boron, *Critical Reviews in Food Science and Nutrition,* 2003, 43, 219-231
38 Forrest H. Nielsen, *Biofactors*, 2004, 20, 161–171
39 Xin Liu, Wenhai Huang, Hailuo Fu, Aihua Yao, Deping Wang, Haobo Pan, William W. Lu, *J Mater Sci: Mater Med*, 2009, 20, 365–372
40 Aihua Yao, Deping Wang, and Wenhai Huang, Qiang Fu and Mohamed N. Rahaman, Delbert E. Day, *J Am Ceram Soc*, 2007, 90, 303 – 306
41 Roger F. Brown, Moha med N. Rahaman, Agat ha B. Dw ilewicz, Wenhai Huang, Delbert E. Day, Yadong Li, B. Sonny Ba, *Journal of Biomedical Materials Research Part A*, 2008, 88, 392-400
42 Xue Han, Delbert E. Day, J Mater Sci: Mater Med, 2007, 18, 1837-1847
43 M. Marezio, J. P. Remeika and P. D. Dernier, *Acta Cryst.,*1969, B25, 965-970
44 M. Marezio, J. P. Remeika and P. D. Dernier, *Acta Cryst.* 1969, B25, 955-964
44 W. H. Zachariasen, *Proceedings of the National Academy of Sciences*, 1931, 17, 617-619.
45 M. Marezio, H. A. Plettinger and W. H. Zachariasen, *Acta Crystallographica*, 1963, 16, 390-392.
46 Y. Fujimoto, T. Yanagida, N. Kawaguchi, S. Kurosawa, K. Fukuda, D. Totsuka, *Cryst Growth Des*, 2012, 12, 142-146.
47 J. H. Hao and J. Gao, *Appl Phys Lett*, 2004, 85, 3720-3722.
48 K. Machida, G. Adachi, J. Shiokawa, M. Shimada, M. Koizumi, *Inorg Chem*, 1980, 19, 983-992.
49 J. L. Huang, L. Y. Zhou, Q. Pang, F. Z. Gong, J. H. Sun, W. Wang, *Lumin*, 2009, 24, 363-366.
50 H. S. Huang and Z. H. Liu, *Mater Res Bull*, 2014, 49, 88-93.
51 W. N. Zhao, Z. M. Xu, T. Y. Sun, X. H. Wu, S. S. Liu, Z. C. Ma, *Solid State Commun*, 2014, 178, 42-45.
52 A. A. Al-Munajjed, N. A. Plunkett, J. P. Gleeson, T. Weber, C. Jungreuthmayer, T. Levingstone, F. J. O'Brien, *J Biomed Mater Res B*, 2009, 90B, 584-591.
53 T. Kokubo and H. Takadama, *Biomater*, 2006, 27, 2907-2915.
54 H. Fisher and R. Marx, *Dent Mater*, 2002, 18, 12-19.
55 A. C. Larson, R. B. Von Dreele, *Los Alamos National Laboratory Report LAUR (Los Alamos National Laboratory Los Alamos, NM)*, 1994, 86-748.
56 A. Takada, C. R. A. Catlow, G. D. Price, C. L. Hayward, *Phys Chem Miner*, 1997, 24, 423-431.
57 S. Mann, B. R. Heywood, S. Rajam, J. D. Birchall, *Nature*, 1988, 334, 692-695.
58 B. R. Judd, *Phys Rev*, 1962, 127, 750-761.
59 G. S. Ofelt, *J Chem Phys*, 2004, 37, 511-520.
60 C. Görller-Walrand and K. Binnemans, *Elsevier Science*, 1996, pp. 121-283.
61 G. Blasse, *Chem Phys Lett*, 1973, 20, 573-574.
62 R. A. S. Ferreira, S. S. Nobre, C. M. Granadeiro, H. I. S. Nogueira, L. D. Carlos, O. L. Malta, *J Lumin*, 2006, 121, 561-567.
63 Y. L. Huang and H. J. Seo, *Mater Lett*, 2012, 84, 107-109.
64 R. Skaudzius, A. Katelnikovas, D. Enseling, A. Kareiva, T. Jüstel, *J Lumin*, 2014, 147, 290-294.
65 A. Baran, J. Barzowska, M. Grinberg, S. Mahlik, K. Szczodrowski, Y. Zorenko, *Opt Mater*, 2013, 35, 2107-2114.
66 S. H. M. Poort, A. Meyerink and G. Blasse, *J Phys Chem Solids*, 1997, 58, 1451-1456.
57 O. Graeve, R. Kanakala, A. Madadi, B. C. Williams, K. C. Glass, *Biomater*, 2010, 31, 4259-4267.

68 Z. Q. Feng, Y. D. Li, Y. L. Huang, H. J. Seo, *J Alloys Compds*, 2011, 509, 7087-7092.
69 T. Kokubo, H. M. Kim, M. Kawashita, T. Nakamura, *J Mater Sci Mater Med*, 2004, 15, 99-107.
70 T. Kokubo, H. Kushitani, C. Ohtsuki, S. Sakka, T. Yamamuro, *Mater Sci Mater Med*, 1993, 4, 1-4.
71 C. Ohtsuki, T. Kokubo and T. Yamamuro, *J Non-Cryst Solids*, 1992, 143, 84-89.
72 K. Sudarsanan and R. A. Youner, *Acta Crystallogr. B*, 1969, 25, 1534-1543.
73 B. Piriou, D. Fahmi, J. Dexpert-Ghys, A. Taitai, and J. L. Lacout, *J. Lumin.*, 1987, 39, 97-103.
74 C. Meis, J. D. Gale, L. Boyer, J. Carpena, and D. Gosset, *J. Phys. Chem. A*, 2000, 104, 5380-5387.
75 S. Body, *Mineralogia*, 2009, 40, 85-94.